ARMY RESEARCH LABORATORY

A Fast Algorithm for Computing Scattered Fields Using Physical Optics Equivalent Approximation in Half-Space

T. Raju Damarla

ARL-TR-2132 July 2000

Approved for public release; distribution unlimited.

The findings in this report are not to be construed as an official Department of the Army position unless so designated by other authorized documents.

Citation of manufacturer's or trade names does not constitute an official endorsement or approval of the use thereof.

Destroy this report when it is no longer needed. Do not return it to the originator.

Army Research Laboratory

Adelphi, MD 20783-1197

ARL-TR-2132 **July 2000**

A Fast Algorithm for Computing Scattered Fields Using Physical Optics Equivalent Approximation in Half-Space

T. Raju Damarla

Sensors and Electron Devices Directorate

Approved for public release; distribution unlimited.

Abstract

In this report, a fast algorithm for computing scattered fields with the use of physical optics (PO) equivalent approximation in half-space is presented. The theoretical basis for the algorithm and the derivation of formulas used in the algorithm is presented. The algorithm is used to compute the radar cross sections (RCSs) of several objects. The RCS of the objects computed by the algorithm is compared with those that were computed with the method of moments (MOM). The results presented are found to be accurate when the target dimensions are greater than or equal to 2λ, where λ denotes the wavelength. It is concluded that the PO algorithm presented in this report can be used for majority of applications as it captured all the salient features of the targets.

Contents

Figures

1. Introduction

In general, scattered fields from complex objects are computed in the frequency domain with the use of the method of moments (MOM). Although this method computes the scattered fields accurately, the computational complexity is shown[1] to be $O(n^3)$, where n is the number of elements for which currents need to be computed. Because of the exponential nature of the computational complexity, as n increases, the use of MOM for computing scattered fields becomes less and less attractive. Other techniques for computing frequency domain scattered fields exist, namely, the fast multipole method (FMM), multilevel FMM, etc. The multilevel FMM techniques have the complexity $O(n \log n)$.[1] Within the realm of MOM, other techniques exist that take advantage of target geometry, such as exploiting body of revolution (BOR) symmetry to reduce the size of matrixes, which must be inverted. In spite of great advances in computational electromagnetics, computing the scattered fields from an arbitrary target can be prohibitive, especially as the target is electrically large. However, at higher frequencies for targets with dimensions greater than 2λ, where λ denotes the wavelength, computing scattered fields by physical optics (PO) approximations yield relatively accurate results. Some of the commercially available high-frequency modeling packages, such as XPATCH, model targets in free space with or without conducting ground planes. The PO code that was developed computes the scattered fields in a lossy and dispersive half-space via the layered medium dyadic Green's function specialized for a half-space. This capability is of interest for simulating targets in real soil. The PO code allows one to compute the radar cross section (RCS) and scattered fields of an arbitrary target that is underground, above ground, or partially buried.

Section 2 presents the basic formulation of the PO approximations and the Green's functions used. Section 3 presents some of the RCS characteristics of various targets, namely, a sphere, a vertical plate, a mine, and an unexploded ordnance (UXO), that were computed with both MOM and PO for comparison. Section 3 also presents some of the actual synthetic aperture radar (SAR) images of UXOs along with the images generated by the simulated data by PO. These images show that most of the salient features of the targets are captured, which in turn, help develop automatic target detection (ATD) and automatic target recognition (ATR) algorithms.

[1] N. Geng, A. Sullivan, and L. Carin, "Fast multipole method for scattering from 3-D PEC targets situated in a half-space environment," *Microwave Opt. Tech. Let.* **21**, No. 6 (June 1999), 399–405.

2. Scattering of Radiation by an Object in Free Space

One assumes that the observations are made in the far field; that is, ($\beta r >> 1$), where $\beta = \omega\sqrt{\mu\varepsilon}$ and μ and ε represent the permeability and permittivity of free space, respectively; β is the wave number; and r denotes the distance from the target to the observation point. Figure 1 shows the coordinate system used for computing scattered fields in the far field. I approximate the distance R from any point on the object to the observation point by

$$R = \begin{cases} r - r' \cos\psi & \text{for phase variations ,} \\ r & \text{for amplitude variations ,} \end{cases} \tag{1}$$

where ψ is the angle between the vectors r and r' (vectors are denoted by bold letters). Then the electric and magnetic fields radiated by the object in the far field are given by

$$\begin{aligned} \mathbf{E}_A &= -j\omega\mathbf{A} \quad (\theta \text{ and } \phi \text{ components only}) \text{ ,} \\ \mathbf{H}_F &= -j\omega\mathbf{F} \quad (\theta \text{ and } \phi \text{ components only}) \text{ ,} \end{aligned} \tag{2}$$

where

$$\mathbf{A} = \frac{\mu}{4\pi}\int\int_S \mathbf{J}_s \frac{e^{-j\beta R}}{R}\, ds \simeq \frac{\mu e^{-j\beta r}}{4\pi r}\mathbf{N} \text{ , and} \tag{3}$$

$$\mathbf{N} = \int\int_S \mathbf{J}_s \exp(j\beta r' \cos\psi)\, ds \text{ ,} \tag{4}$$

Figure 1. Coordinate system for radiation by an object.

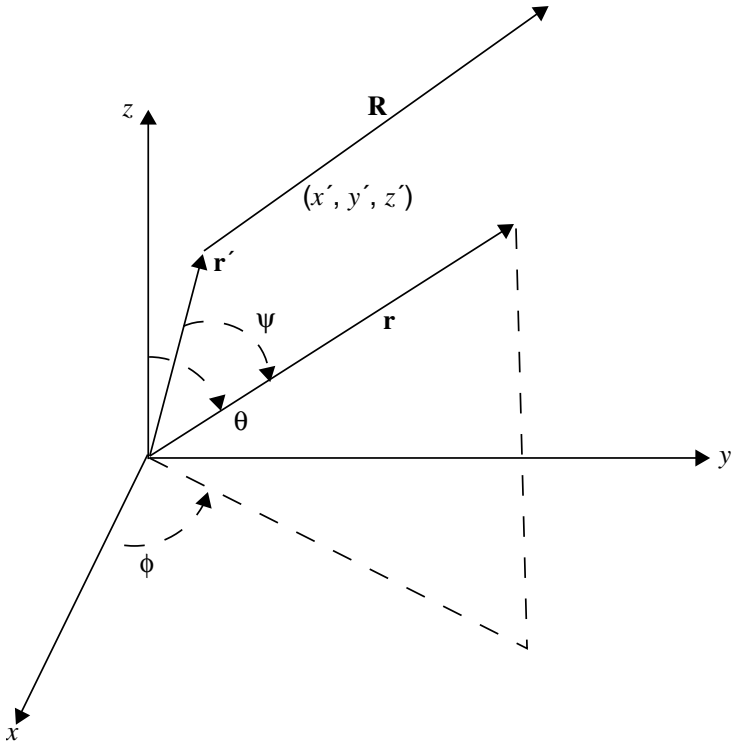

where $\mathbf{J}_s$ and $\mathbf{M}_s$ denote the electric and magnetic current densities induced on the object. Clearly, scattered field $\mathbf{E}$ can be computed if $\mathbf{J}_s$ is known. To compute $\mathbf{J}_s$ in an object, one assumes a known plane wave is impinging on the object. PO approximation gives a relation between the induced magnetic field and the current density $\mathbf{J}_s$. The following subsection presents the relevant concepts.

2.1 Physical Optics Equivalent

For the sake of completeness, I present in this subsection a brief description of PO approximation theory. Detailed explanation and derivation of relevant formulation can be found in literature by Balanis.[2]

Let us consider an unbounded medium with constituting parameters ε_1 and μ_1. Let us also assume that a current source $\mathbf{J}_1$ radiating $\mathbf{E}_1$ and a magnetic current source $\mathbf{M}_1$ radiating $\mathbf{H}_1$ are everywhere in the medium. Moreover, consider an imaginary region V_1 enclosed by a surface S_1 in this medium as shown in figure 2. Assume that the surface S_1 is replaced by another medium with parameters ε_2 and μ_2. Let us also assume that the sources $\mathbf{J}_1$ and $\mathbf{M}_1$ are allowed to radiate in the presence of the new medium in V_1. The total field outside the region V_1, produced by $\mathbf{J}_1$ and $\mathbf{M}_1$, is $\mathbf{E}$ and $\mathbf{H}$ and inside V_1 is $\mathbf{E}^t$ and $\mathbf{H}^t$.

The total field outside the region V_1 is equal to the original field ($\mathbf{E}_1$ and $\mathbf{H}_1$) in the absence of the obstacle plus a perturbation (scattered) field ($\mathbf{E}^s$, $\mathbf{H}^s$), introduced by the obstacle. Hence,

$$\begin{aligned} \mathbf{E} &= \mathbf{E}_1 + \mathbf{E}^s \ , \\ \mathbf{H} &= \mathbf{H}_1 + \mathbf{H}^s \ . \end{aligned} \tag{5}$$

In the above equation, one can compute the original fields $\mathbf{E}_1$ and $\mathbf{H}_1$ by solving Maxwell's equations. To compute $\mathbf{E}^s$ and $\mathbf{H}^s$, I introduce boundary currents $\mathbf{J}_p$ and $\mathbf{M}_p$ on the surface.

These currents can be expressed in terms of the difference in fields ($\mathbf{E}^s$, $\mathbf{H}^s$) that are outside the region V_1 and the fields ($\mathbf{E}^t$, $\mathbf{H}^t$) that are inside the region V_1 as follows:

$$\begin{aligned} \mathbf{J}_p &= \hat{n} \times \left(\mathbf{H}^s - \mathbf{H}^t \right) \ , \\ \mathbf{M}_p &= -\hat{n} \times \left(\mathbf{E}^s - \mathbf{E}^t \right) \ , \end{aligned} \tag{6}$$

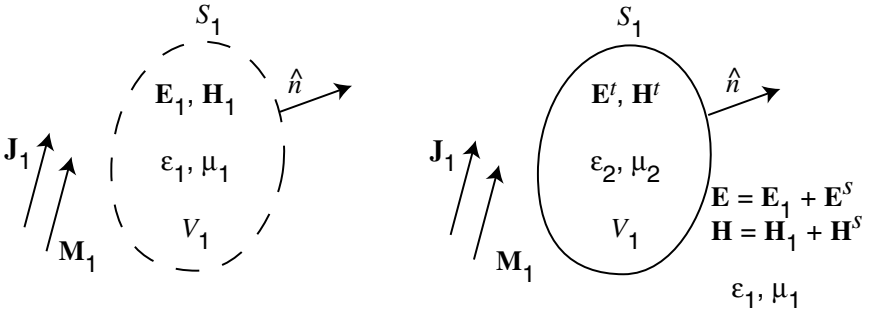

Figure 2. Field geometry for derivation of currents on a surface of an object.

[2] C. A. Balanis, *Advanced Engineering Electromagnetics*, John Wiley and Sons, Inc., New York, NY (1989).

where "×" denotes the cross product. Since the tangential components of **E** and **H** must be continuous across the boundary, I get

$$\begin{aligned} \mathbf{E}_1|_{\tan} + \mathbf{E}^s|_{\tan} &= \mathbf{E}^t|_{\tan} \Rightarrow \hat{n} \times (\mathbf{E}_1 + \mathbf{E}^s) = \hat{n} \times \mathbf{E}^t \ , \\ \mathbf{H}_1|_{\tan} + \mathbf{H}^s|_{\tan} &= \mathbf{H}^t|_{\tan} \Rightarrow \hat{n} \times (\mathbf{H}_1 + \mathbf{H}^s) = \hat{n} \times \mathbf{H}^t \ , \end{aligned} \tag{7}$$

or

$$\begin{aligned} \mathbf{E}^s|_{\tan} - \mathbf{E}^t|_{\tan} &= -\mathbf{E}_1|_{\tan} \Rightarrow \hat{n} \times (\mathbf{E}^s - \mathbf{E}^t) = -\hat{n} \times \mathbf{E}_1 \ , \\ \mathbf{H}^s|_{\tan} - \mathbf{H}^t|_{\tan} &= -\mathbf{H}_1|_{\tan} \Rightarrow \hat{n} \times (\mathbf{H}^s - \mathbf{H}^t) = -\hat{n} \times \mathbf{H}_1 \ . \end{aligned} \tag{8}$$

Substituting equations (8) in (6), I get

$$\begin{aligned} \mathbf{J}_p &= -\hat{n} \times \mathbf{H}_1 \\ \mathbf{M}_p &= \hat{n} \times \mathbf{E}_1 \ . \end{aligned} \tag{9}$$

Let us now assume that the obstacle occupying the region V_1 is a perfect electric conductor (PEC) with conductivity $\sigma = \infty$. Then the fields in the region $\mathbf{E}^t$ and $\mathbf{H}^t$ equal zero as shown in figure 3. Over the boundary S_1 of the conductor, the total tangential components of the **E** field are equal to zero, and the total tangential components of the **H** field are equal to the induced current density $\mathbf{J}_p$. Hence,

$$\mathbf{M}_p = -\hat{n} \times (\mathbf{E} - \mathbf{E}^t) = -\hat{n} \times \mathbf{E} = -\hat{n} \times (\mathbf{E}_1 + \mathbf{E}^s) = 0 \ ,$$

or

$$\begin{aligned} -\hat{n} \times \mathbf{E}_1 &= \hat{n} \times \mathbf{E}^s \ , \text{ and} \\ \mathbf{J}_p &= \hat{n} \times (\mathbf{H} - \mathbf{H}^t) = \hat{n} \times \mathbf{H} = \hat{n} \times (\mathbf{H}_1 + \mathbf{H}^s) \ , \end{aligned} \tag{10}$$

or for an infinitely large object, it can be shown by image theory[2] that $\mathbf{H}_1|_{\tan} = \mathbf{H}^s|_{\tan}$. Hence, the PO for equation (10) becomes

$$\begin{aligned} \mathbf{J}_p &= 2\hat{n} \times \mathbf{H}_1 \ \text{ in the lit region and} \\ \mathbf{J}_p &= 0 \qquad\quad \text{in the shadow region} \ . \end{aligned} \tag{11}$$

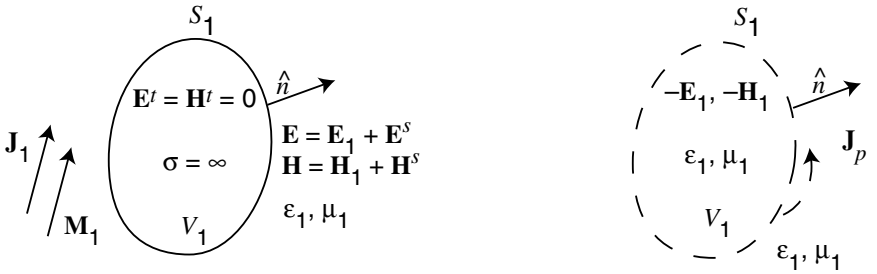

Figure 3. Field geometry for physical optics approximation.

[2]C. A. Balanis, *Advanced Engineering Electromagnetics*, John Wiley and Sons, Inc., New York, NY (1989).

Equation (11) allows us to compute the current density $\mathbf{J}_p$ on the target because of $\mathbf{H}_1$, which one assumes can be computed. Once we have determined $\mathbf{J}_p$, we can use equations (2) to (4) to compute the field radiated by the target with current density $\mathbf{J}_p$. In particular, the scattered field can be computed once $\bar{N}$ in equation (4) is determined; namely,

$$\mathbf{N} = \iint_S \mathbf{J} \exp(j\beta r' \cos\psi)\, ds = \iint_S \mathbf{J} \exp(j\beta \mathbf{r} \cdot \mathbf{r}')\, ds \ , \tag{12}$$

where "$\cdot$" denotes the dot product. Note that $\mathbf{J}$ in equation (12) is computed by equation (11). Expanding equation (12) in terms of its x, y, and z components of the current $\mathbf{J}$ produces

$$\mathbf{N} = \iint_S \left(\hat{a}_x J_x + \hat{a}_y J_y + \hat{a}_z J_z\right) \exp(j\beta \mathbf{r} \cdot \mathbf{r}')\, ds \ . \tag{13}$$

Using the rectangular-to-spherical component transformation, where

$$\begin{bmatrix} \hat{a}_x \\ \hat{a}_y \\ \hat{a}_z \end{bmatrix} = \begin{bmatrix} \sin\theta\ \cos\phi & \cos\theta\ \cos\phi & -\sin\phi \\ \sin\theta \sin\phi & \cos\theta \sin\phi & \cos\phi \\ \cos\theta & -\sin\theta & 0 \end{bmatrix} \begin{bmatrix} \hat{a}_r \\ \hat{a}_\theta \\ \hat{a}_\phi \end{bmatrix} , \tag{14}$$

we can write the θ (vertical polarization) and ϕ (horizontal polarization) components of $\mathbf{N}$ as

$$N_\theta = \iint_S \left(J_x \cos\theta \cos\phi + J_y \cos\theta \sin\phi - J_z \sin\theta\right) \exp(j\beta \mathbf{r} \cdot \mathbf{r}')\, ds \ , \tag{15}$$

$$N_\phi = \iint_S \left(J_x \sin\phi + J_y \cos\phi\right) \exp(-j\beta \mathbf{r} \cdot \mathbf{r}')\, ds \ . \tag{16}$$

Using equations (15) and (16) in equations (2) and (3) produces expressions for scattered field in vertical and horizontal polarizations:

vertical polarization

$$E_\theta = -\frac{j\omega\mu}{4\pi r} e^{-j\beta r} \iint_S \left(J_x \cos\theta \cos\phi + J_y \cos\theta \sin\phi - J_z \sin\theta\right) \times \exp\left[j\beta(x' \sin\theta \cos\phi + y' \sin\theta \sin\phi + z' \cos\theta)\right] ds \tag{17}$$

horizontal polarization

$$E_\phi = -\frac{j\omega\mu}{4\pi r} e^{-j\beta r} \iint_S \left(-J_x \sin\phi + J_y \cos\phi\right) \times \exp[j\beta(x' \sin\theta \cos\phi + y' \sin\theta \sin\phi + z' \cos\theta)]\, ds \tag{18}$$

Note that equations (17) and (18) correspond to the scattered fields in free space. The following section presents the half-space approximations. We can obtain these approximations by incorporating the half-space dyadic Green's functions.*

*T. Dogaru, private notes, Electrical Engineering Dept., Duke University, Durham, NC.

2.2 Half-Space Approximations

Consider two layers with an xy-plane with $z = 0$ as the boundary between the two as shown in figure 4. The medium in layer 1 has the permittivity ε_1 and permeability μ_1 while the medium in layer 2 has ε_2 and μ_2. Often the medium in layer 1 is air; thus, $\mu_1 = \mu_0 = 4\pi 10^{-7}$ H/m and $\varepsilon_1 = \varepsilon_0 = 10^{-9}/36\pi$ F/m. Define the following functions:

$$\beta_1 = \omega\sqrt{\mu_1\varepsilon_1} \ ,$$

$$\beta_2 = \omega\sqrt{\mu_2\varepsilon_2} \ ,$$

$$\exp_1 = \exp[j\beta_1(x'\sin\theta\cos\phi + y'\sin\theta\sin\phi + z'\cos\theta)] \ ,$$

$$\exp_2 = \exp[j\beta_1(x'\sin\theta\cos\phi + y'\sin\theta\sin\phi - z'\cos\theta)] \ ,$$

$$\exp_3 = \exp\left[j\left(\beta_1(x'\sin\theta\cos\phi + y'\sin\theta\sin\phi) + z'\sqrt{\beta_2^2 - (\beta_1\sin\theta)^2}\right)\right] \ ,$$

$$T_{xx} = T_{yy} = \frac{2\beta_1\cos\theta}{\beta_1\cos\theta + \sqrt{\beta_2^2 - (\beta_1\sin\theta)^2}} \ ,$$

$$T_{zz} = \frac{2\beta_1\cos\theta}{\frac{\beta_2^2}{\beta_1}\cos\theta + \sqrt{\beta_2^2 - (\beta_1\sin\theta)^2}} \ ,$$

$$T_{zx} = \left(\frac{\frac{\beta_2^2}{\beta_1}\cos\theta - \sqrt{\beta_2^2 - (\beta_1\sin\theta)^2}}{\frac{\beta_2^2}{\beta_1}\cos\theta + \sqrt{\beta_2^2 - (\beta_1\sin\theta)^2}} + \frac{\beta_1\cos\theta - \sqrt{\beta_2^2 - (\beta_1\sin\theta)^2}}{\beta_1\cos\theta + \sqrt{\beta_2^2 - (\beta_1\sin\theta)^2}}\right)\frac{\cos\theta\cos\phi}{\sin\theta} \ ,$$

$$T_{zy} = T_{zx}\frac{\sin\phi}{\cos\phi} \ ,$$

$$R_{xx} = R_{yy} = \frac{\beta_1\cos\theta - \sqrt{\beta_2^2 - (\beta_1\sin\theta)^2}}{\beta_1\cos\theta + \sqrt{\beta_2^2 - (\beta_1\sin\theta)^2}} \ ,$$

$$R_{xx} = R_{yy} = \frac{\beta_1\cos\theta - \sqrt{\beta_2^2 - (\beta_1\sin\theta)^2}}{\beta_1\cos\theta + \sqrt{\beta_2^2 - (\beta_1\sin\theta)^2}} \ ,$$

$$R_{zx} = T_{zx} \ ,$$

$$R_{zy} = R_{zx}\frac{\sin\phi}{\cos\phi} \ .$$

Figure 4. Geometry used for layered medium.

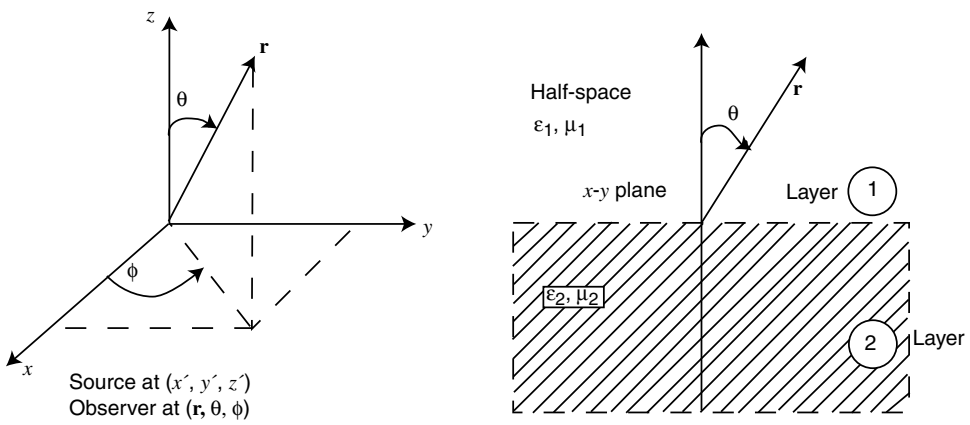

The following are the expressions for E_θ and E_ϕ for the target in layer 1:

$$E_\theta = \frac{-j\omega\mu_1}{4\pi r} e^{-j\beta_1 r} \iint_S \left(J_x [\cos\theta \cos\phi (\exp_1 + R_{xx} \exp_2) - \sin\theta R_{zx} \exp_2] \right.$$
$$\left. + J_y [\cos\theta \sin\phi (\exp_1 + R_{yy} \exp_2) - \sin\theta R_{zy} \exp_2] - J_z \sin\theta (\exp_1 + R_{zz} \exp_2) \right) ds \ , \quad (19)$$

$$E_\phi = -\frac{j\omega\mu_1}{4\pi r} e^{-j\beta_1 r} \iint_S \left(-J_x \sin\phi (\exp_1 + R_{xx} \exp_2) + J_y \cos\phi (\exp_1 + R_{yy} \exp_2) \right) ds \ . \quad (20)$$

Expressions for E_θ and E_ϕ for the target in layer 2 are given by

$$E_\theta = -\frac{j\omega\mu_1}{4\pi r} e^{-j\beta_1 r} \iint_S \left(J_x (\cos\theta \cos\phi \, T_{xx} - \sin\theta \, T_{zx}) \exp_3 \right.$$
$$\left. + J_y (\cos\theta \sin\phi \, T_{yy} - \sin\theta \, T_{zy}) \exp_3 - J_z \sin\theta \, T_{zz} \exp_3 \right) ds \ , \quad (21)$$

$$E_\phi = -\frac{j\omega\mu_1}{4\pi r} e^{-j\beta_1 r} \iint_S \left(-J_x \sin\phi \, T_{xx} \exp_3 + J_y \cos\phi \, T_{yy} \exp_3 \right) ds \ . \quad (22)$$

Equations (19) to (22) can be used for computing the scattered fields by a target.

2.3 Implementation of PO Approximations in Half-Space for Computation of Scattered Fields

To compute the scattered fields near a target, one must first partition the target into small triangles with each side of the triangle approximately 0.1λ, where λ denotes the wavelength. For each triangle patch, an outward normal and its centroid are computed. This normal is used to compute the current induced by a magnetic field in the patch. The centroid becomes the reference point in the patch for computing electric and magnetic fields. The magnetic field in a patch is then used to determine the current with the use of PO approximation. Once the current in a patch is computed, it is then used to compute the electrical field radiated (scattered field) by the patch. The sum total of all the fields radiated by all the patches constitutes the scattered field by the target.

Now to compute the induced current caused by a magnetic field, let us assume that an incident plane wave where the electric field has a magnitude $E_0 = 1$ is impinging on the target. Let the direction of the incident plane wave be given by θ and ϕ; then the unit-transmitted vector in rectangular-coordinate system is given by

layer 1: $\mathbf{t_x} = -[\sin\theta\cos\phi, \sin\theta\sin\phi, \cos\theta]$

$$\mathbf{r} = |r|\,\mathbf{t_x}\ ,$$

and the reflected vector is $\mathbf{r_1} = -[\sin\theta\cos\phi, \sin\theta\sin\phi, -\cos\theta]$, and

layer 2: $\mathbf{t_x} = -[\sin\theta_t\cos\phi, \sin\theta_t\sin\phi, \cos\theta_t]$,

where θ_t denotes the angle of refraction in medium 2 and is determined by Snell's law: $\sin\theta_t = \beta_1 \sin\theta/\beta_2$.

Figure 5 shows the transmitted, reflected, and refracted rays (vectors) and the corresponding angles.

Field computations in layer 1:

The electric fields in vertical and horizontal polarizations impinging on a patch are given by

transmitted field

$$\begin{aligned}\mathbf{E}_V &= E_0[\cos\theta\cos\phi, \cos\theta\sin\phi, -\sin\theta]\exp[-j\beta_1(\mathbf{t_x}\cdot\mathbf{P}_i)]\ ,\\ \mathbf{E}_H &= E_0[-\sin\phi, \cos\phi, 0]\exp[-j\beta_1(\mathbf{t_x}\cdot\mathbf{P}_i)]\ ,\end{aligned} \tag{23}$$

where $\mathbf{P}_i = [x_i, y_i, z_i]$ denotes the coordinates of the centroid of an ith triangular patch of the target.

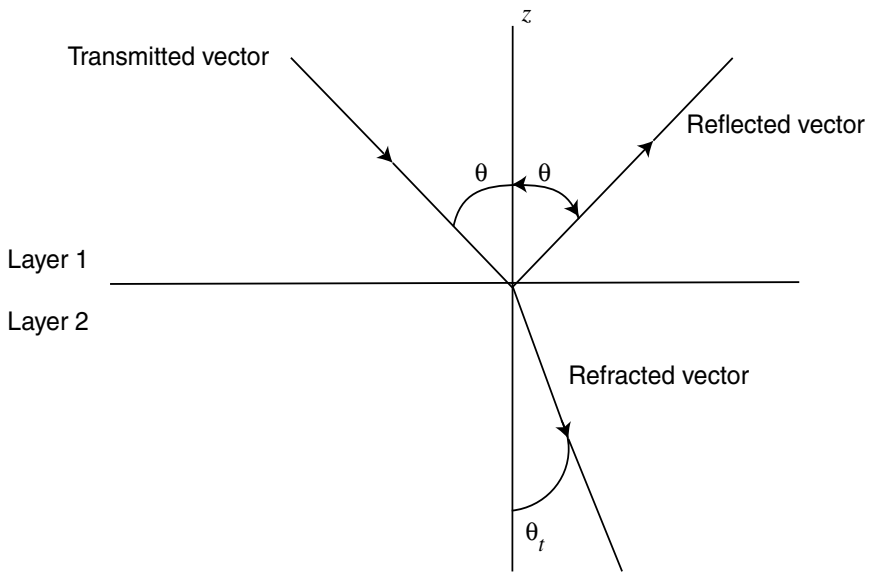

Figure 5. Ray dynamics.

reflected field

$$\mathbf{E}_V^r = (E_0 r_v)[\cos\theta\cos\phi, \cos\theta\sin\phi, \sin\theta]\exp[-j\beta_1(\mathbf{r_1}\cdot\mathbf{P}_i)] \ ,$$
$$\mathbf{E}_H^r = (E_0 r_h)[-\sin\phi, \cos\phi, 0]\exp[-j\beta_1(\mathbf{r_1}\cdot\mathbf{P}_i)] \ , \tag{24}$$

where the reflection coefficients r_v and r_h are given by

$$r_v = \frac{\eta_2\cos\theta_t - \eta_1\cos\theta}{\eta_2\cos\theta_t + \eta_1\cos\theta} \ ,$$

$$r_h = \frac{\eta_2\cos\theta - \eta_1\cos\theta_t}{\eta_2\cos\theta + \eta_1\cos\theta_t}$$

and

$$\eta_1 = \sqrt{\frac{\mu_1}{\varepsilon_1}} \ \text{ intrinsic impedance of medium 1} \ ,$$

$$\eta_2 = \frac{\eta_1}{\sqrt{\varepsilon_2}} \quad \text{intrinsic impedance of medium 2} \ .$$

Then the magnetic fields can be expressed in terms of the electric fields as

$$\mathbf{H}_V = \frac{1}{\eta_1}(\mathbf{t_x}\times\mathbf{E}_V) \ ,$$
$$\mathbf{H}_H = \frac{1}{\eta_1}(\mathbf{t_x}\times\mathbf{E}_H) \ ,$$
$$\mathbf{H}_V^r = \frac{1}{\eta_1}(\mathbf{r_1}\times\mathbf{E}_V^r) \ , \tag{25}$$
$$\mathbf{H}_H^r = \frac{1}{\eta_1}(\mathbf{r_1}\times\mathbf{E}_H^r) \ ,$$

where $\mathbf{a}\times\mathbf{b}$ represents the cross product between two vectors **a** and **b**.

Computation of currents in a triangular patch:

Having determined the magnetic fields in a triangular patch, I can now compute the currents using the PO approximation given by equation (11) as follows:

$$\mathbf{J}_V = 2(\hat{\mathbf{n}}_P\times\mathbf{H}_V)$$
$$\mathbf{J}_H = 2(\hat{\mathbf{n}}_P\times\mathbf{H}_H)$$
$$\mathbf{J}_V^r = 2(\hat{\mathbf{n}}_P\times\mathbf{H}_V^r) \tag{26}$$
$$\mathbf{J}_H^r = 2(\hat{\mathbf{n}}_P\times\mathbf{H}_H^r) \ ,$$

where $\hat{\mathbf{n}}_P$ denotes the outward normal to the triangular patch P. Note that the normal $\hat{\mathbf{n}}_P$ and the $\mathbf{H}_V$ should correspond to the same triangular

patch. Now I can compute the scattered fields using equations (19) and (20). Note that equation (19) gives the scattered field in vertical polarization. By using $\mathbf{J}_V$, the current caused by the vertically polarized transmitted field in equations (19) and (20), I can obtain scattered fields in vertical transmit, vertical receive (VV) and vertical transmit, horizontal receive (VH) polarizations. Similarly, using $\mathbf{J}_H$ in equations (19) and (20), I can obtain scattered fields in HV and HH polarizations:

$$\mathbf{E}_{VV} = -\frac{j\omega\mu_1}{4\pi R}e^{-j\beta_1 R}\iint_S (J_{Vx}[\cos\theta\cos\phi(\exp_1 + R_{xx}\exp_2) - \sin\theta R_{zx}\exp_2] + J_{Vy}[\cos\theta\sin\phi(\exp_1 + R_{yy}\exp_2) - \sin\theta R_{zy}\exp_2] - J_{Vz}\sin\theta(\exp_1 + R_{zz}\exp_2))ds \ , \tag{27}$$

$$\mathbf{E}_{VH} = -\frac{j\omega\mu_1}{4\pi R}e^{-j\beta_1 R}\iint_S (-J_{Vx}\sin\phi(\exp_1 + R_{xx}\exp_2) + J_{Vy}\cos\phi(\exp_1 + R_{yy}\exp_2))\,ds \ , \tag{28}$$

$$\mathbf{E}_{HV} = -\frac{j\omega\mu_1}{4\pi R}e^{-j\beta_1 R}\iint_S (J_{Hx}[\cos\theta\cos\phi(\exp_1 + R_{xx}\exp_2) - \sin\theta R_{zx}\exp_2] + J_{Hy}[\cos\theta\sin\phi(\exp_1 + R_{yy}\exp_2) - \sin\theta R_{zy}\exp_2] - J_{Hz}\sin\theta(\exp_1 + R_{zz}\exp_2)\,ds \ , \tag{29}$$

$$\mathbf{E}_{HH} = -\frac{j\omega\mu_1}{4\pi R}e^{-j\beta_1 R}\iint_S (-J_{Hx}\sin\phi(\exp_1 + R_{xx}\exp_2) + J_{Hy}\cos\phi(\exp_1 + R_{yy}\exp_2))\,ds \ , \tag{30}$$

where $\mathbf{J}_V = [J_{Vx}, J_{Vy}, J_{Vz}]$ and R is the distance between the observation point and the target. Similarly, $\mathbf{E}^r_{VV}$, $\mathbf{E}^r_{VH}$, $\mathbf{E}^r_{HV}$, and $\mathbf{E}^r_{HH}$ can be computed with similar equations (eq. (27) to (30)), where $\mathbf{J}_V$ and $\mathbf{J}_H$ are replaced by $\mathbf{J}^r_V$ and $\mathbf{J}^r_H$, respectively. These scattered electric fields are computed for only those triangle patches illuminated by either $\mathbf{t_x}$ or $\mathbf{r_l}$. The sum of $\mathbf{E}_{VV} + \mathbf{E}^r_{VV}$ for all the illuminated patches gives the scattered electric field in VV polarization. Similarly, other summations give the field in VH, HV, and HH polarizations.

Computations in layer 2:

Field computations in layer 2 are as follows:

$$\mathbf{E}_V = (E_0 \cdot \mathbf{T}_V)[\cos\theta_t\cos\phi, \cos\theta_t\sin\phi, -\sin\theta_t]\exp[-j\beta_1(\mathbf{t_x}\cdot\mathbf{P}_i)] \ ,$$
$$\mathbf{E}_H = (E_0\mathbf{T}_H)[-\sin\phi, \cos\phi, 0]\exp[-j\beta_1(\mathbf{t_x}\cdot\mathbf{P}_i)] \ , \tag{31}$$

where

$$\mathbf{t_x} = -[\sin\theta_t\cos\phi, \sin\theta_t\sin\phi, \cos\theta_t] \ ,$$

and the transmission coefficients $\mathbf{T}_V$ and $\mathbf{T}_H$ are given by

$$\mathbf{T}_V = \frac{2\eta_2 \cos\theta}{\eta_2 \cos\theta_t + \eta_1 \cos\theta}$$

$$\mathbf{T}_H = \frac{2\eta_2 \cos\theta}{\eta_2 \cos\theta + \eta_1 \cos\theta_t} \ .$$

Notice that no reflected fields are in layer 2. As in layer 1, magnetic fields and currents in each triangular patch are computed, and the scattered fields are computed with equations (27) to (30) and appropriate currents.

3. Validation of PO Code

A PO code was implemented in a matrix laboratory (MATLAB) environment. To verify the accuracy of the code, I created several targets and computed their RCSs using both PO code and MOM code. The MOM code is developed by Duke University. The comparison results are presented below.

Vertical plate: A 1-m^2 plate was created as shown in figure 6 and placed 0.15 m above the Eglin soil with permittivity of $\varepsilon_r = 5.0 - j0.0$ and conductivity of $\sigma = 0.003$. For the computation of the scattered fields at various frequencies, an incident field at $\theta = 45°$ and $\phi = 0°$ was used. The plate was oriented to get the dihedral effect from the ground. I computed the RCS characteristics of the plate from 25 to 2000 MHz. The results are shown in figures 7 and 8 for VV and HH polarizations, respectively.

Figures 7 and 8 show that PO output is fairly accurate compared to that of the actual output computed by MOM at frequencies 600 MHz and higher. In other words, when the target was greater than or equal to 2λ, I obtained good correlation with the MOM simulations. Why the PO output for HH polarization had better correlation at even lower frequencies with MOM output compared to VV polarization is not clear.

The next object I used for simulations and comparison was a horizontal cylinder with a spherical head on one side as shown in figure 9. The dimensions of the cylinder were length = 0.58 m and diameter = 0.078 m. I performed two simulations, namely, a cylinder buried 1 in. below Yuma soil and a cylinder placed 1 in. above Eglin soil. The results of the simulations are shown in figures 10 to 15 for a target buried 1 in. below the surface in Yuma soil. PO output is plotted by a solid line and MOM output is plotted by a dotted line. Notice from these figures that the RCS computed for the cylinder using the PO code is accurate. The largest difference between the MOM and PO code is observed in figure 15, where $\phi = -90°$; at that angle, it is known[2] that PO does not do well. Figures 16 to 21 show the RCS characteristics of a cylinder placed 1 in. above the surface of Eglin soil.

First, I simulated the scattering fields for the cylinder shown in figure 9 for all azimuthal angles $\phi = 0°$ to 360° and generated SAR images using the back-projection algorithm. The SAR images generated using MOM and PO simulated data are shown in figure 22 for a cylinder buried 1 in. below the surface of Yuma soil. From the SAR images, I found that an excellent correlation exists between the MOM and PO simulated SAR images in terms of resolution and that both the images have similar magnitudes. Next, I used a UXO (shown in fig. 23), which was buried in Yuma soil. I made actual measurements of the UXO using a radar. Its SAR images and the PO simulated images for the same UXO are presented in figure 24. It shows that the SAR images using PO simulated data can capture all the features of the UXO. This helps in developing ATD and ATR algorithms for various targets.

[2]C. A. Balanis, *Advanced Engineering Electromagnetics*, John Wiley and Sons, Inc., New York, NY (1989).

Figure 6. A 1- × 1-m^2 plate.

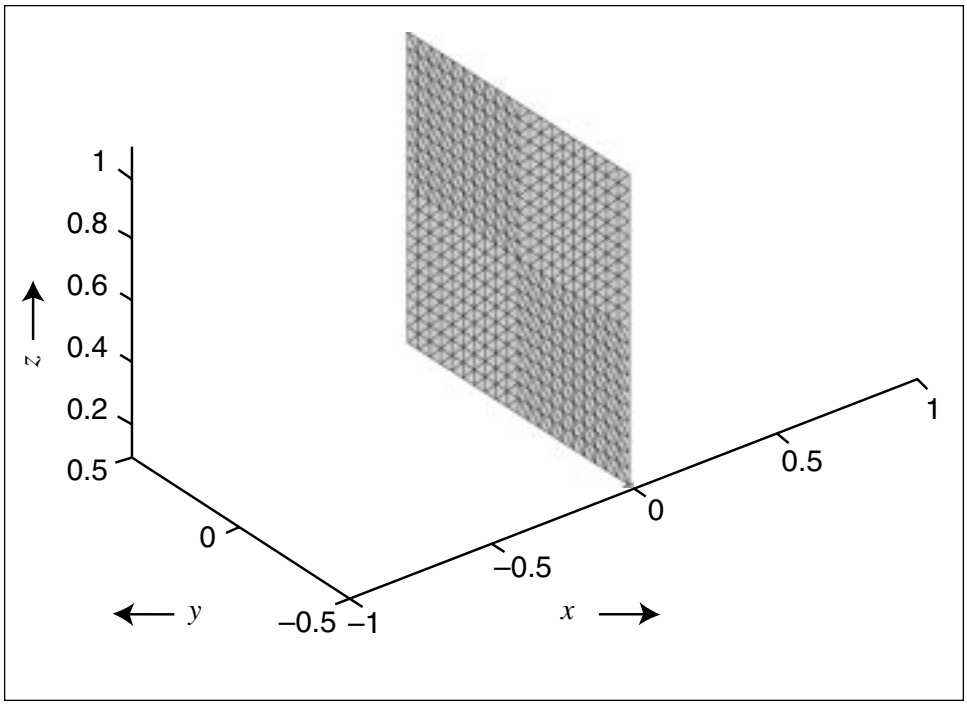

Figure 7. RCS VV characteristics of a plate in a half-space.

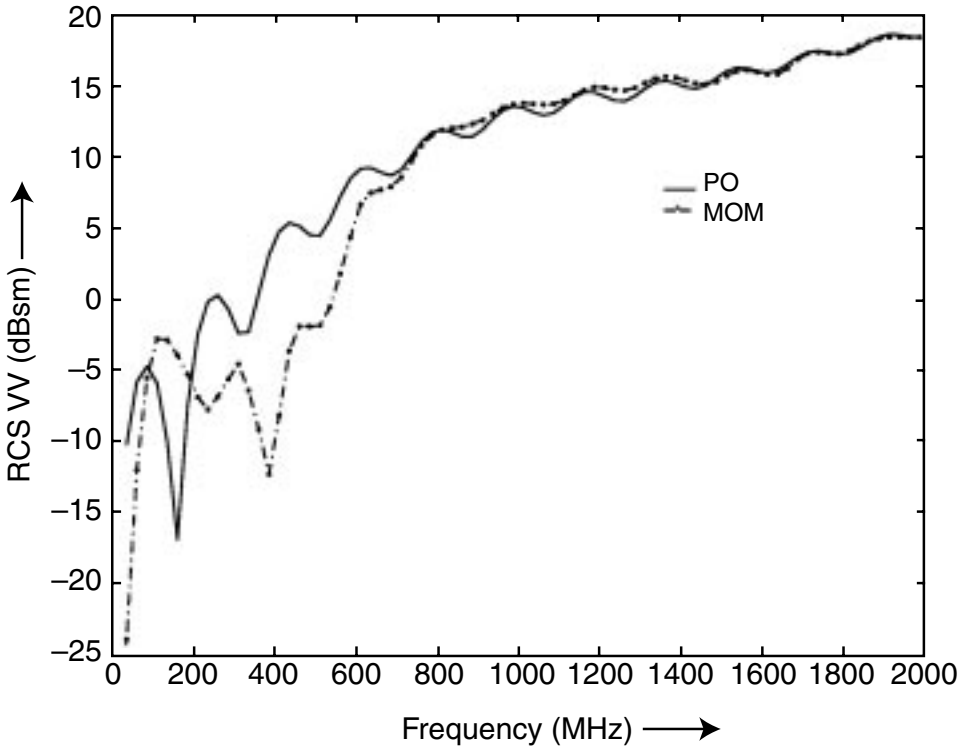

Figure 8. RCS HH characteristics of a plate in a half-space.

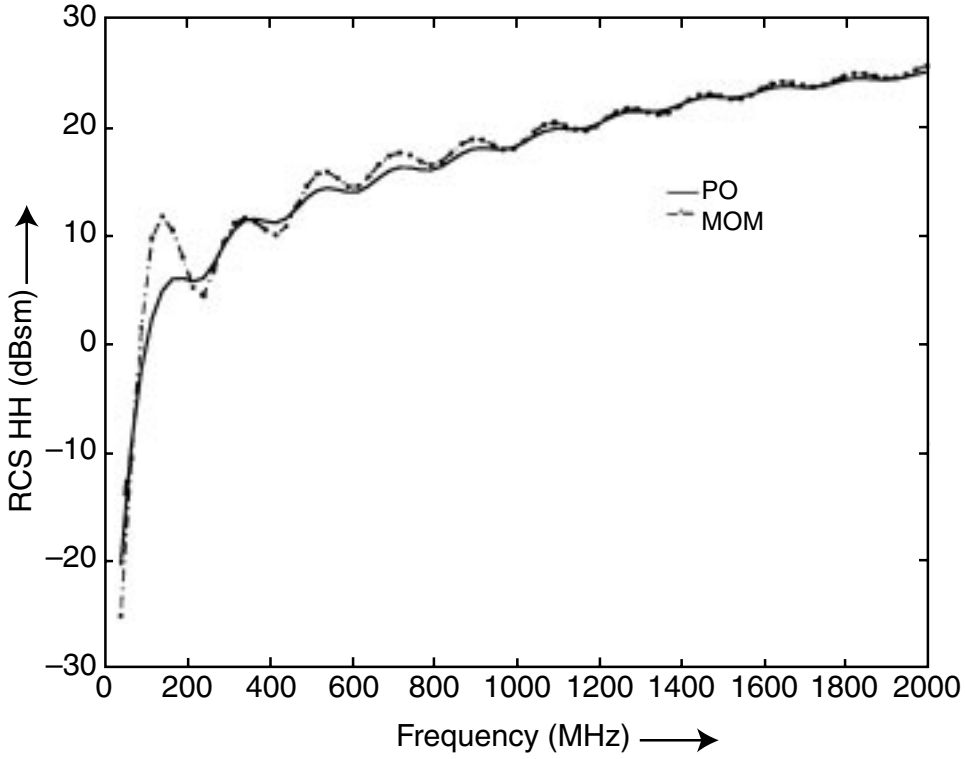

Figure 9. Cylindrical target used.

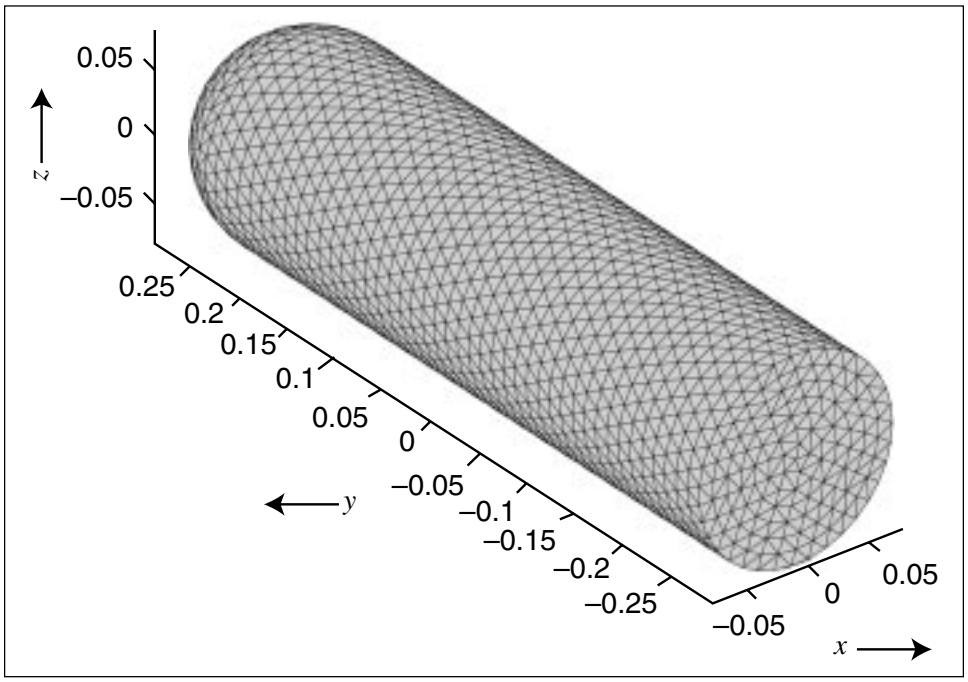

Figure 10. RCS VV of a cylinder, $\theta = 60^\circ$, $\phi = 0^\circ$ (broadside).

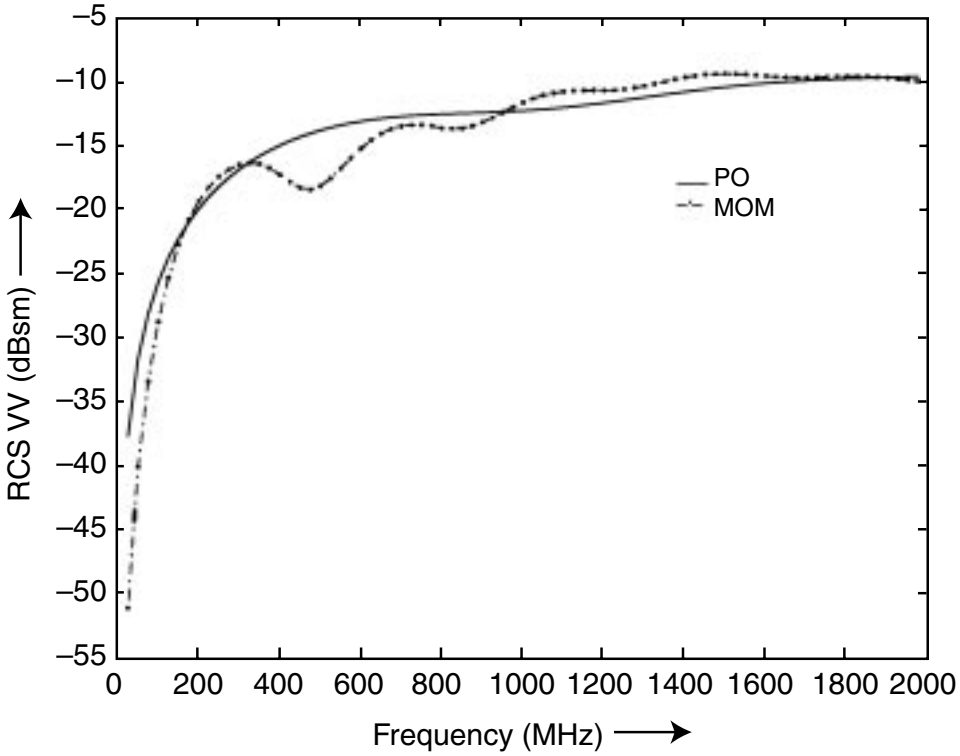

Figure 11. RCS HH of a cylinder, $\theta = 60^\circ$, $\phi = 0^\circ$ (broadside).

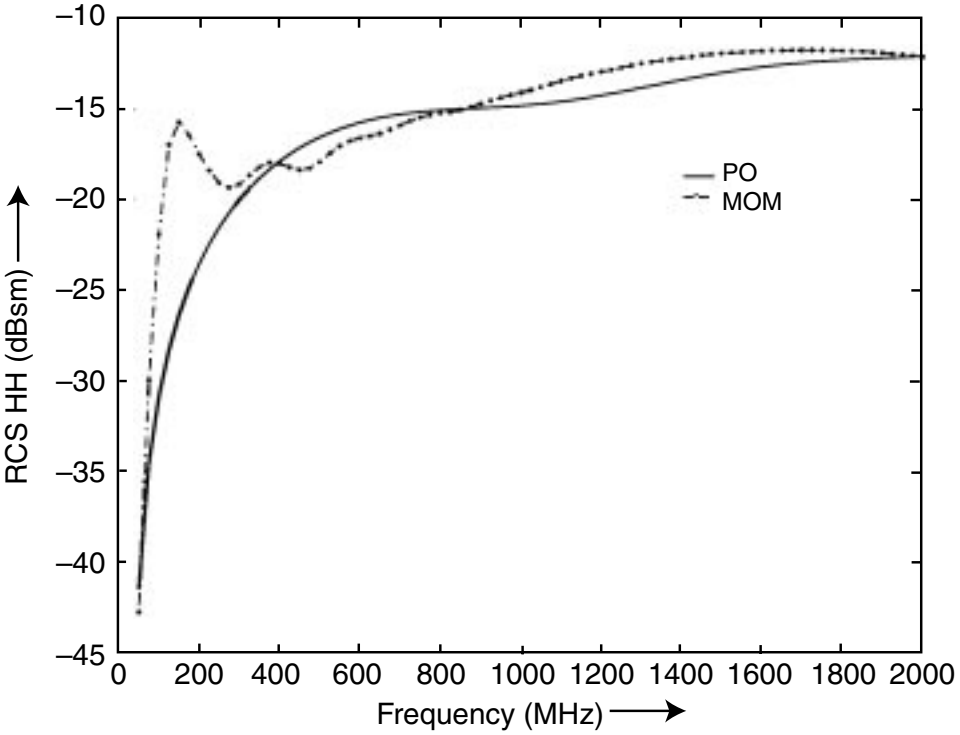

Figure 12. RCS VV of a cylinder, $\theta = 60^\circ$, $\phi = 45^\circ$ (off axis).

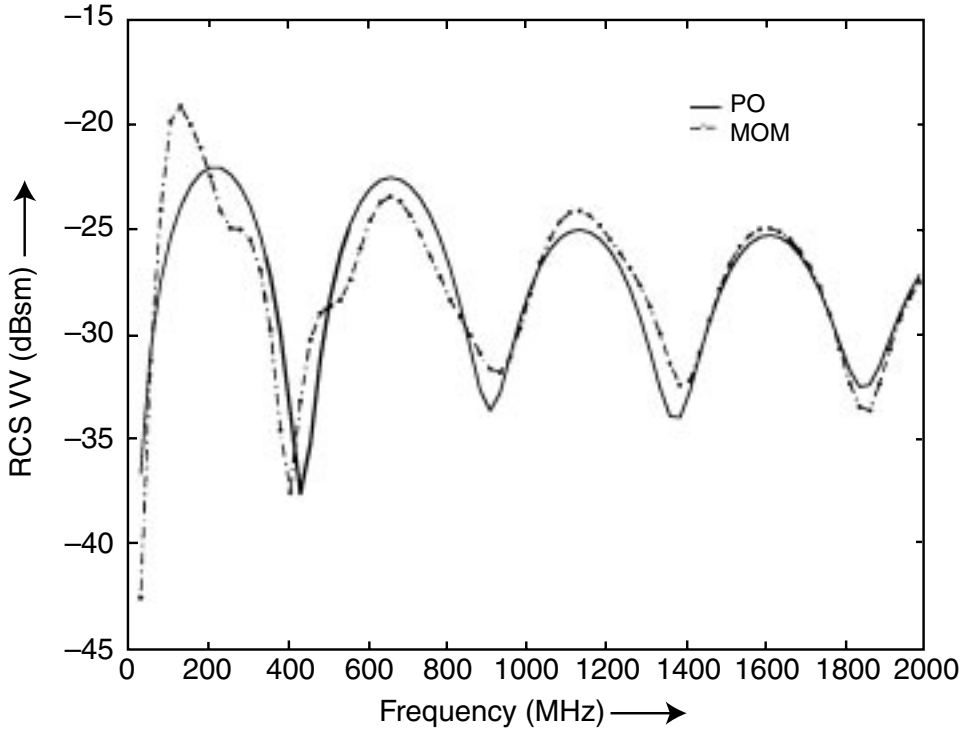

Figure 13. RCS VV of a cylinder, $\theta = 60^\circ$, $\phi = 45^\circ$ (off axis).

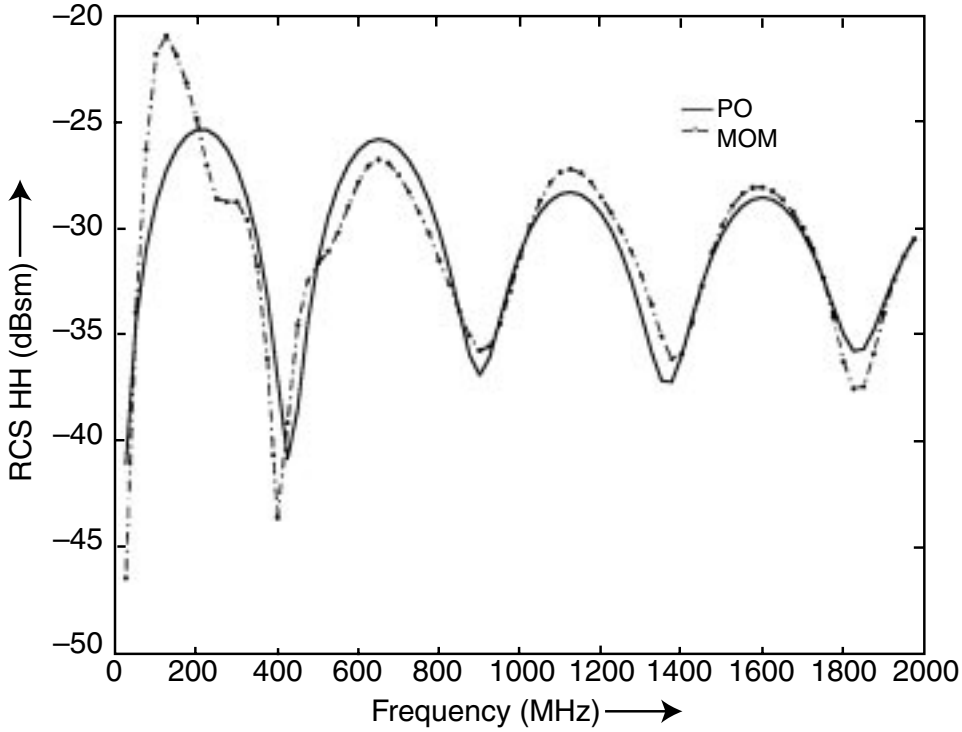

Figure 14. RCS VV of a cylinder, $\theta = 60^\circ$, $\phi = -90^\circ$ (axial).

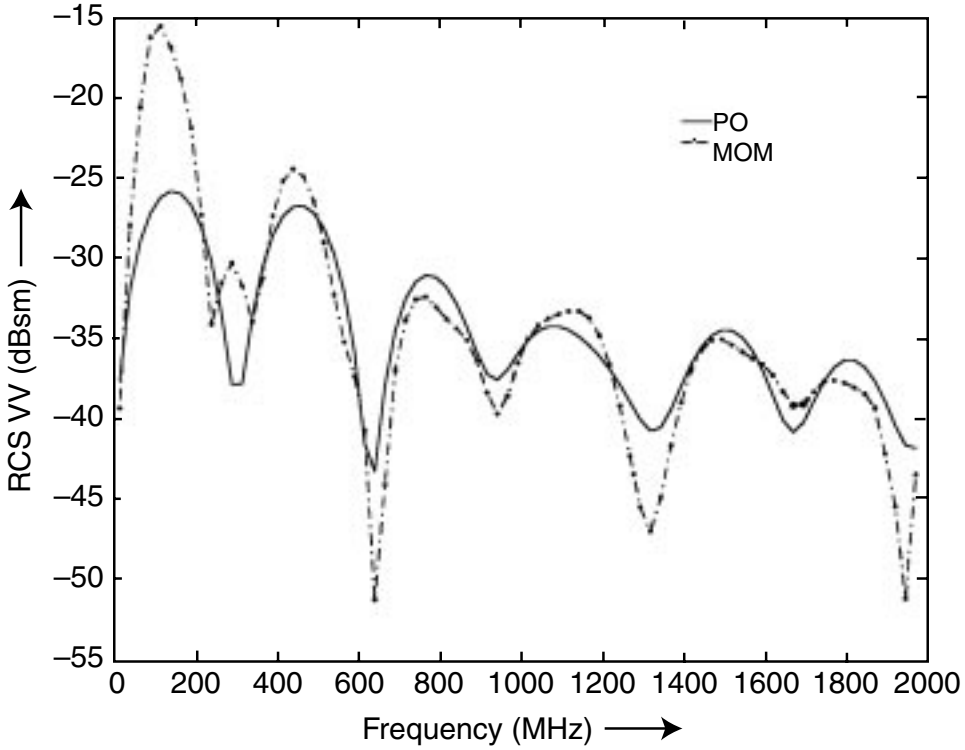

Figure 15. RCS HH of a cylinder, $\theta = 60^\circ$, $\phi = -90^\circ$ (axial).

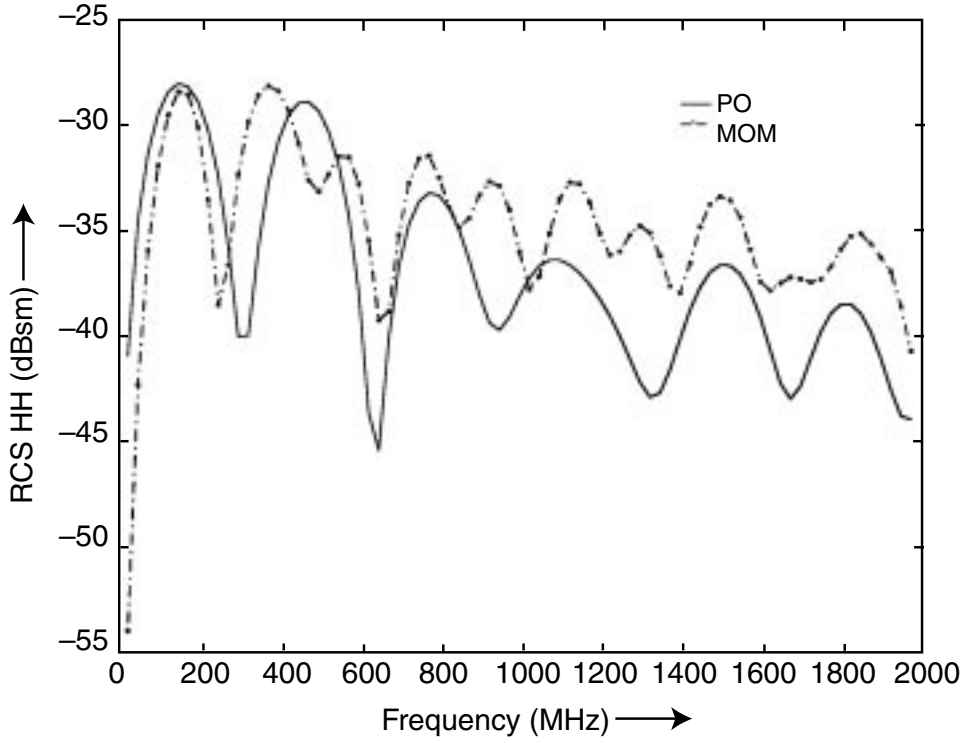

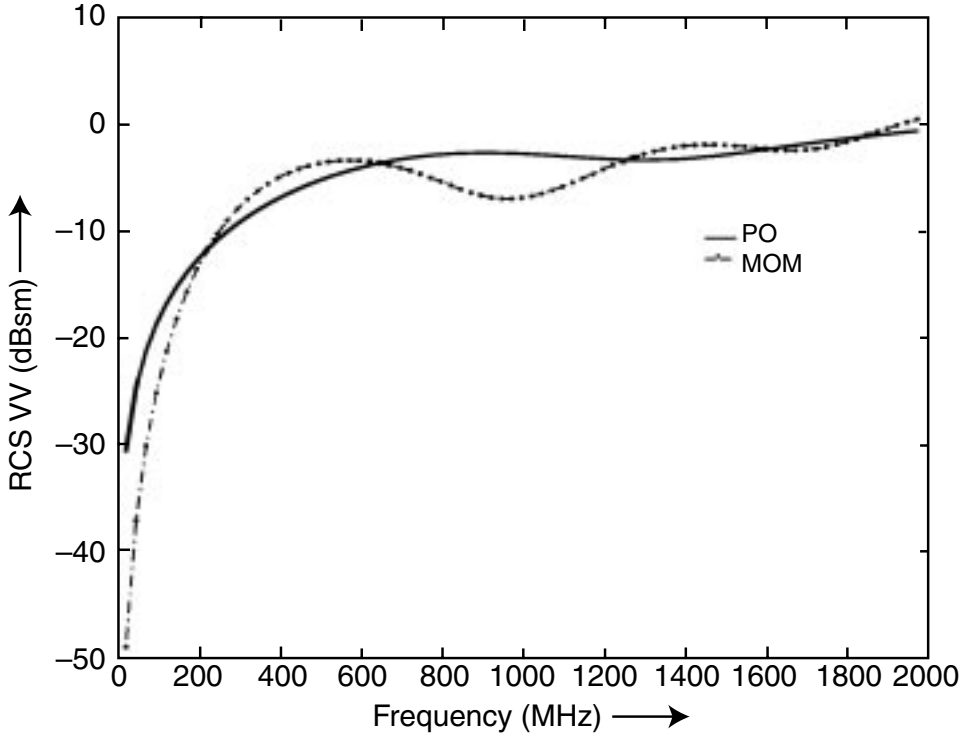

Figure 16. RCS VV of a cylinder above Eglin soil, $\theta = 60^\circ$, $\phi = 0^\circ$ (broadside).

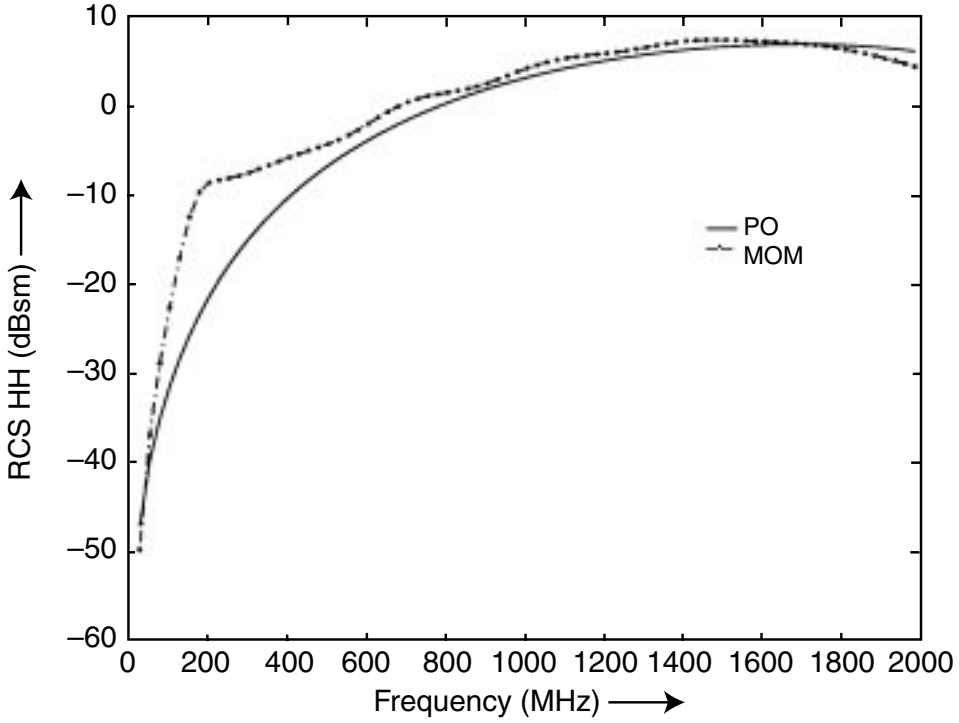

Figure 17. RCS HH of a cylinder above Eglin soil, $\theta = 60^\circ$, $\phi = 0^\circ$ (broadside).

Figure 18. RCS VV of a cylinder above Eglin soil, $\theta = 60^\circ$, $\phi = 45^\circ$ (off axis).

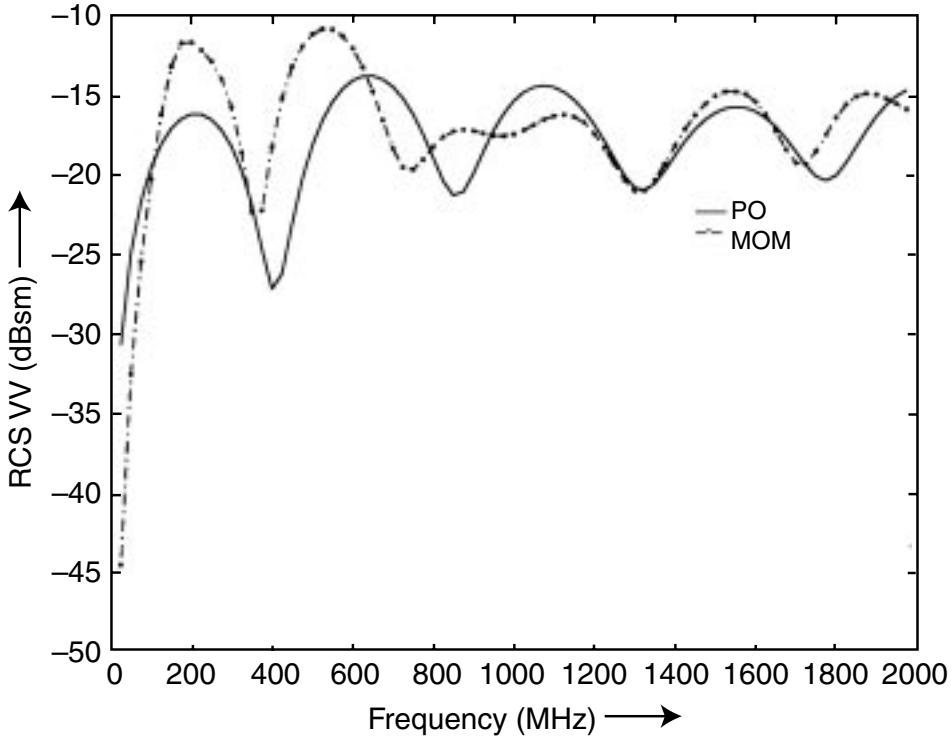

Figure 19. RCS HH of a cylinder above Eglin soil, $\theta = 60^\circ$, $\phi = 45^\circ$ (off axis).

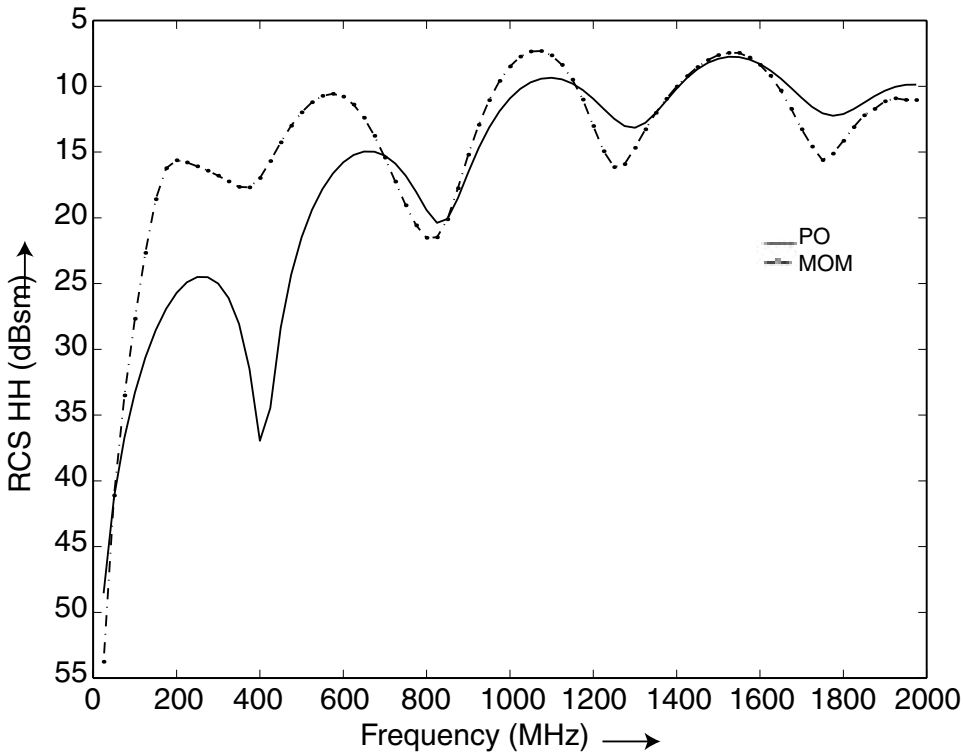

Figure 20. RCS VV of a cylinder above Eglin soil, $\theta = 60^\circ$, $\phi = -90^\circ$ (axial).

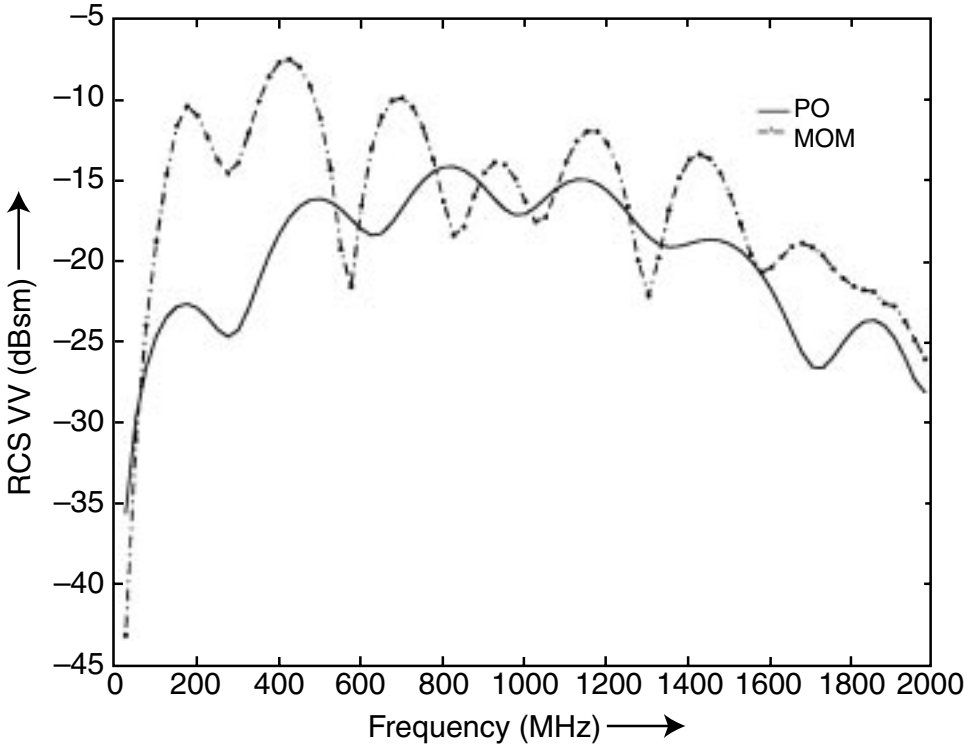

Figure 21. RCS HH of a cylinder above Eglin soil, $\theta = 60^\circ$, $\phi = -90^\circ$ (axial).

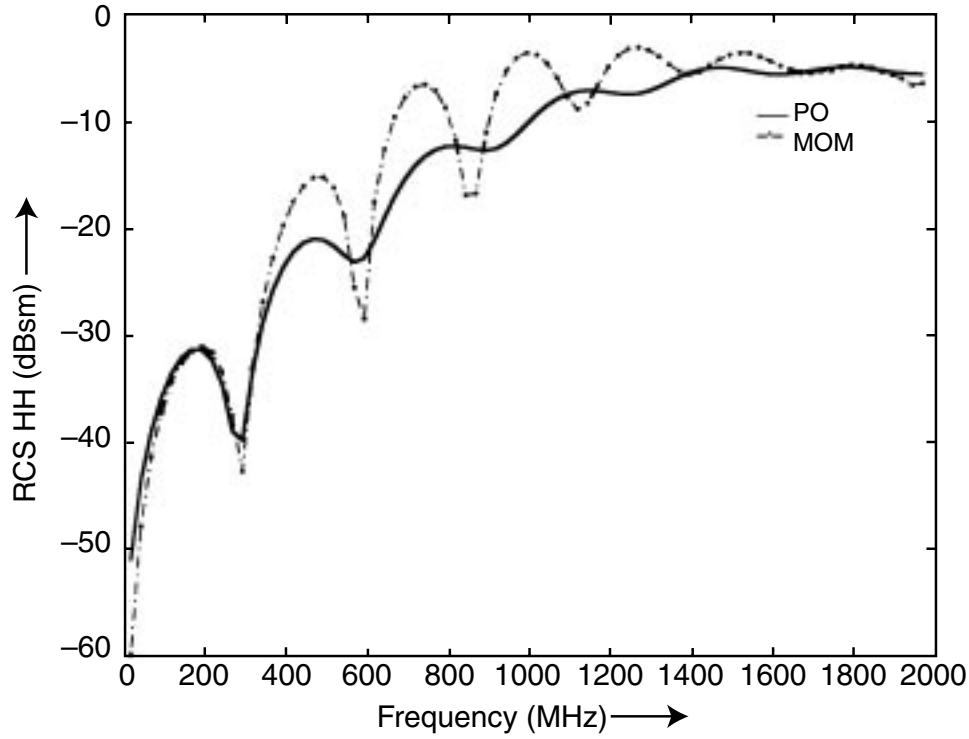

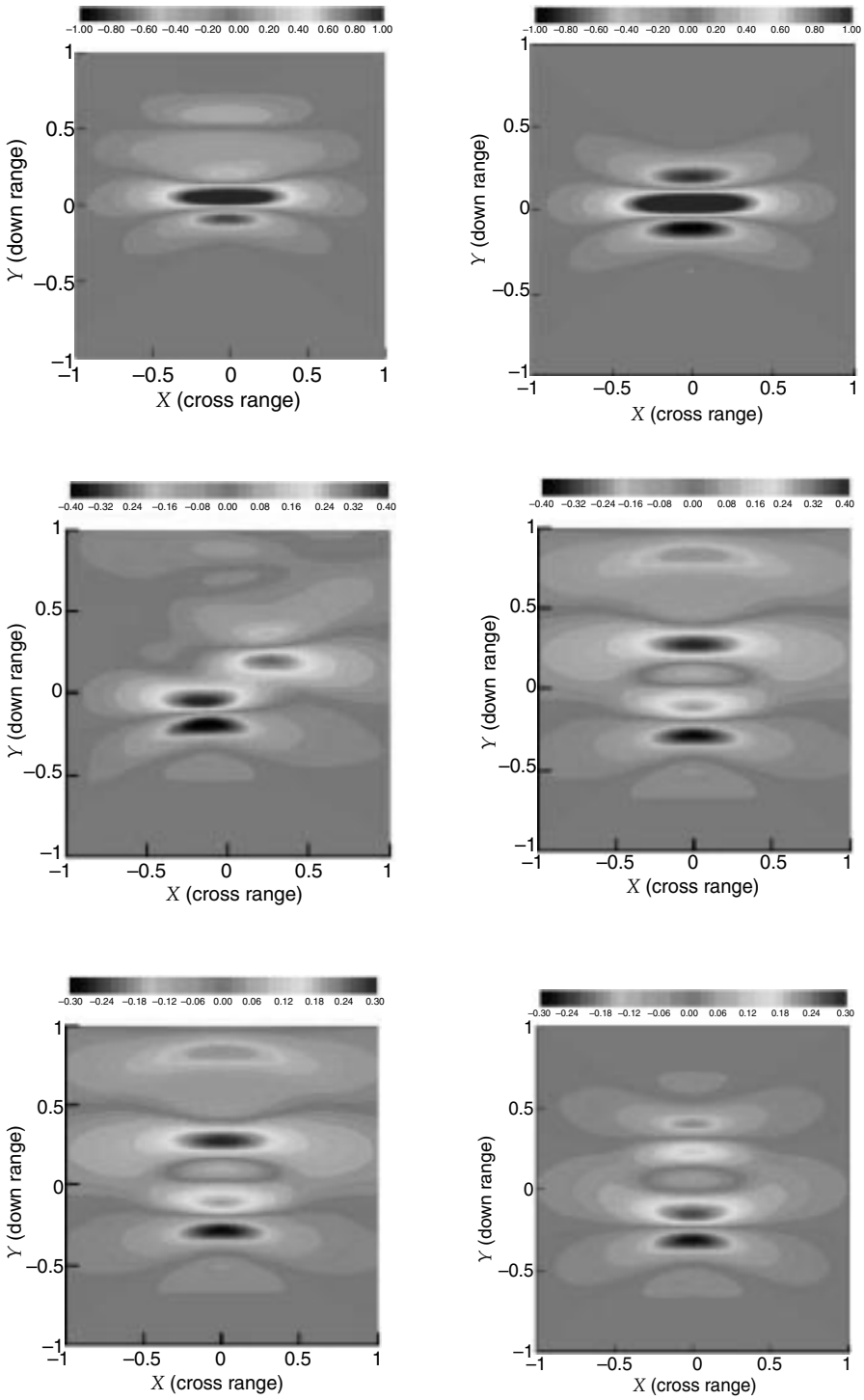

Figure 22. Left column MOM, right column PO. Top row $\phi = 0^\circ$, middle row $\phi = 135^\circ$, bottom row $\phi = -90^\circ$.

Figure 23. UXO used for measurements and simulations.

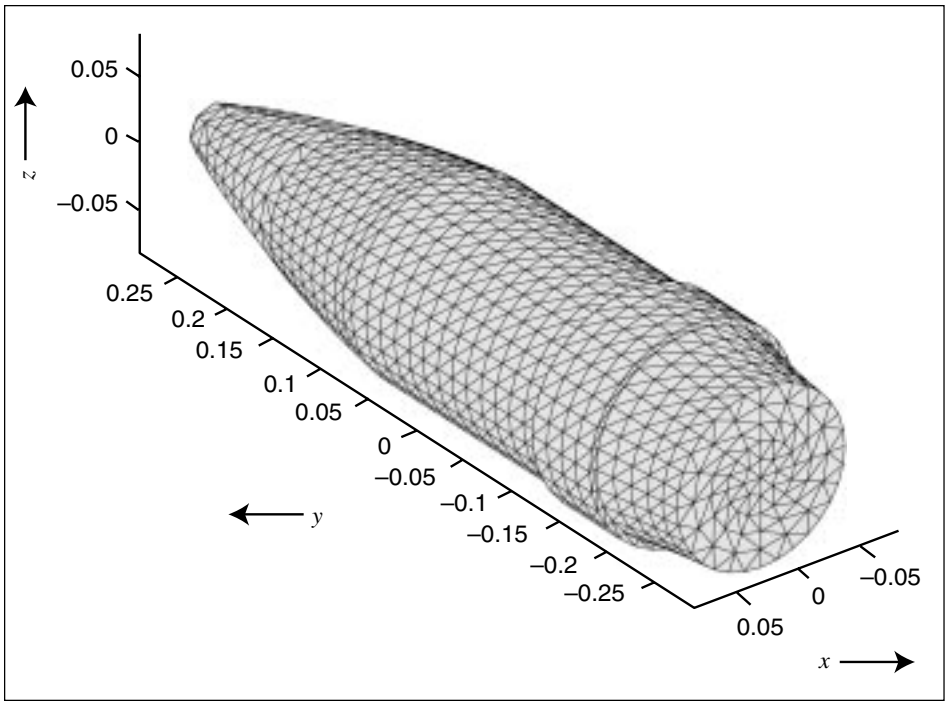

Figure 24. (a) Measured versus (b) simulated SAR images using PO.

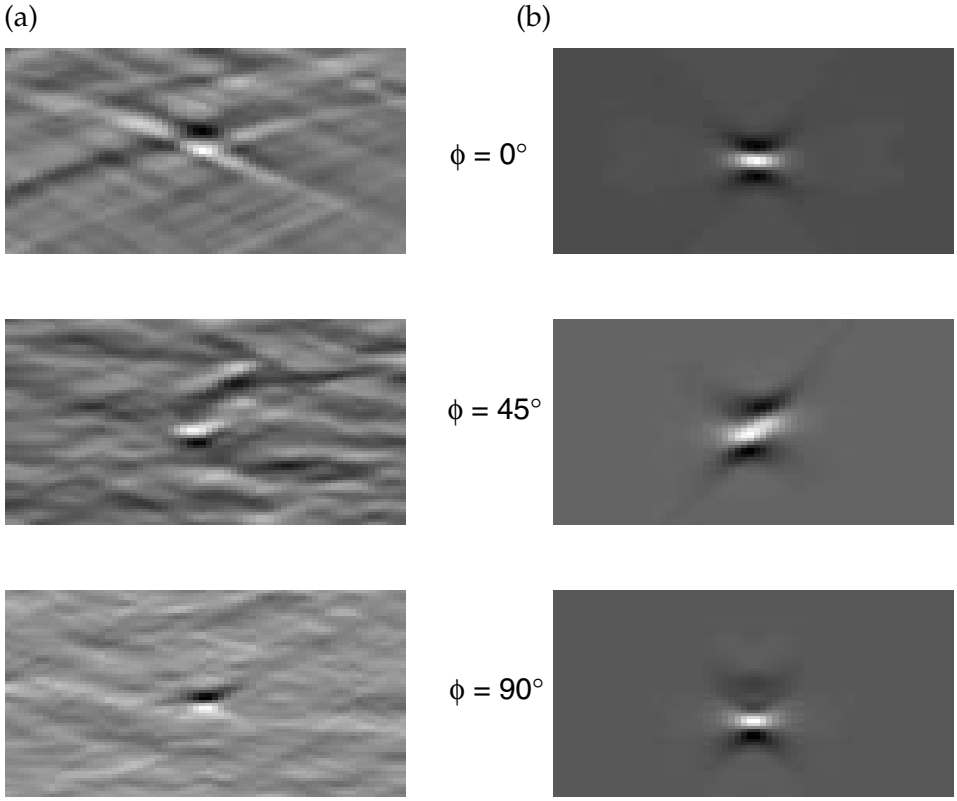

4. Remarks

One of the drawbacks in the current PO code is that normals of various patches are being used to determine whether a patch is illuminated by the transmitted/reflected ray. However, it does not determine whether a patch is blocked by some part of the target. For some simple targets, this is not a problem. If the target is complex and has many corners and projections, the PO code may not give accurate results unless the above-mentioned problem is solved.

Acknowledgments

I would like to acknowledge my sincere appreciation and gratitude to Professor L. Carin for giving me an opportunity to spend six months at Duke University. I also would like to thank Yanting Dong, Duke University, and A. Sullivan, ARL, for their help and discussions.

I would like to thank Jeffrey Sichina, Microwave Branch, and the SEDD management for allowing me to go to Duke University.

Distribution

Admnstr
Defns Techl Info Ctr
Attn DTIC-OCP
8725 John J Kingman Rd Ste 0944
FT Belvoir VA 22060-6218

Ofc of the Secy of Defns
Attn ODDRE (R&AT)
The Pentagon
Washington DC 20301-3080

Ofc of the Secy of Defns
Attn OUSD(A&T)/ODDR&E(R) R J Trew
3080 Defense Pentagon
Washington DC 20301-7100

AMCOM MRDEC
Attn AMSMI-RD W C McCorkle
Redstone Arsenal AL 35898-5240

Dir for MANPRINT
Ofc of the Deputy Chief of Staff for Prsnnl
Attn J Hiller
The Pentagon Rm 2C733
Washington DC 20301-0300

SMC/CZA
2435 Vela Way Ste 1613
El Segundo CA 90245-5500

US Army ARDEC
Attn AMSTA-AR-TD M Fisette
Bldg 1
Picatinny Arsenal NJ 07806-5000

US Army Info Sys Engrg Cmnd
Attn AMSEL-IE-TD F Jenia
FT Huachuca AZ 85613-5300

US Army Natick RDEC Acting Techl Dir
Attn SBCN-T P Brandler
Natick MA 01760-5002

US Army Simulation, Train, & Instrmntn Cmnd
Attn AMSTI-CG M Macedonia
Attn J Stahl
12350 Research Parkway
Orlando FL 32826-3726

US Army Soldier & Biol Chem Cmnd Dir of Rsrch & Techlgy Dirctrt
Attn SMCCR-RS I G Resnick
Aberdeen Proving Ground MD 21010-5423

US Army Tank-Automtv Cmnd Rsrch, Dev, & Engrg Ctr
Attn AMSTA-TR J Chapin
Warren MI 48397-5000

US Army Train & Doctrine Cmnd
Battle Lab Integration & Techl Dirctrt
Attn ATCD-B
FT Monroe VA 23651-5850

US Military Academy
Mathematical Sci Ctr of Excellence
Attn MDN-A LTC M D Phillips
Dept of Mathematical Sci Thayer Hall
West Point NY 10996-1786

Nav Surface Warfare Ctr
Attn Code B07 J Pennella
17320 Dahlgren Rd Bldg 1470 Rm 1101
Dahlgren VA 22448-5100

DARPA
Attn S Welby
3701 N Fairfax Dr
Arlington VA 22203-1714

Hicks & Associates Inc
Attn G Singley III
1710 Goodrich Dr Ste 1300
McLean VA 22102

Palisades Inst for Rsrch Svc Inc
Attn E Carr
1745 Jefferson Davis Hwy Ste 500
Arlington VA 22202-3402

Director
US Army Rsrch Ofc
Attn AMSRL-RO-D JCI Chang
PO Box 12211
Research Triangle Park NC 27709

Distribution (cont'd)

US Army Rsrch Lab
Attn AMSRL-DD J M Miller
Attn AMSRL-CI-AI-R Mail & Records Mgmt
Attn AMSRL-CI-AP Techl Pub (3 copies)

US Army Rsrch Lab (cont'd)
Attn AMSRL-CI-LL Techl Lib (3 copies)
Attn AMSRL-SE-RU R Damarla (40 copies)
Adelphi MD 20783-1197

REPORT DOCUMENTATION PAGE

Form Approved
OMB No. 0704-0188

Public reporting burden for this collection of information is estimated to average 1 hour per response, including the time for reviewing instructions, searching existing data sources, gathering and maintaining the data needed, and completing and reviewing the collection of information. Send comments regarding this burden estimate or any other aspect of this collection of information, including suggestions for reducing this burden, to Washington Headquarters Services, Directorate for Information Operations and Reports, 1215 Jefferson Davis Highway, Suite 1204, Arlington, VA 22202-4302, and to the Office of Management and Budget, Paperwork Reduction Project (0704-0188), Washington, DC 20503.

1. AGENCY USE ONLY *(Leave blank)*	2. REPORT DATE	3. REPORT TYPE AND DATES COVERED
	July 2000	Final,

4. TITLE AND SUBTITLE A Fast Algorithm for Computing Scattered Fields Using Physical Optics Equivalent Approximation in Half-Space

5. FUNDING NUMBERS
DA PR: AH16
PE: 62120A

6. AUTHOR(S) T. Raju Damarla

7. PERFORMING ORGANIZATION NAME(S) AND ADDRESS(ES)
U.S. Army Research Laboratory
Attn: AMSRL-SE-RU email: rdamarla@arl.mil
2800 Powder Mill Road
Adelphi, MD 20783-1197

8. PERFORMING ORGANIZATION REPORT NUMBER
ARL-TR-2132

9. SPONSORING/MONITORING AGENCY NAME(S) AND ADDRESS(ES)
U.S. Army Research Laboratory
2800 Powder Mill Road
Adelphi, MD 20783-1197

10. SPONSORING/MONITORING AGENCY REPORT NUMBER

11. SUPPLEMENTARY NOTES
ARL PR: 0NE4I4
AMS code: 622120.H16

12a. DISTRIBUTION/AVAILABILITY STATEMENT Approved for public release; distribution unlimited.

12b. DISTRIBUTION CODE

13. ABSTRACT *(Maximum 200 words)*

In this report, a fast algorithm for computing scattered fields with the use of physical optics (PO) equivalent approximation in half-space is presented. The theoretical basis for the algorithm and the derivation of formulas used in the algorithm is presented. The algorithm is used to compute the radar cross sections (RCSs) of several objects. The RCS of the objects computed by the algorithm is compared with those that were computed with the method of moments (MOM). The results presented are found to be accurate when the target dimensions are greater than or equal to 2λ, where λ denotes the wavelength. It is concluded that the PO algorithm presented in this report can be used for majority of applications as it captured all the salient features of the targets.

14. SUBJECT TERMS
RCS, MOM

15. NUMBER OF PAGES
33

16. PRICE CODE

17. SECURITY CLASSIFICATION OF REPORT	18. SECURITY CLASSIFICATION OF THIS PAGE	19. SECURITY CLASSIFICATION OF ABSTRACT	20. LIMITATION OF ABSTRACT
Unclassified	Unclassified	Unclassified	UL

NSN 7540-01-280-5500

Standard Form 298 (Rev. 2-89)
Prescribed by ANSI Std. Z39-18
298-102